Friction **9**(6): 1616–1634 (2021)
https://doi.org/10.1007/s40544-020-0447-3
ISSN 2223-7690
CN 10-1237/TH
RESEARCH ARTICLE

Simulation of the fatigue-wear coupling mechanism of an aviation gear

Boyu ZHANG[1], Huaiju LIU[1,*], Caichao ZHU[1], Yibo GE[2]
[1]*State Key Laboratory of Mechancial Transmissions, Chongqing University, Chongqing 400044, China*
[2]*Shanghai Peentech Equipment Tech. Co. Ltd., Shanghai 201800, China*
Received: 31 March 2020 / Revised: 09 July 2020 / Accepted: 21 August 2020

Abstract: The contact fatigue of aviation gears has become more prominent with greater demands for heavy-duty and high-power density gears. Meanwhile, the coexistence of tooth contact fatigue damage and tooth profile wear leads to a complicated competitive mechanism between surface-initiated failure and subsurface-initiated contact fatigue failures. To address this issue, a fatigue-wear coupling model of an aviation gear pair was developed based on the elastic-plastic finite element method. The tooth profile surface roughness was considered, and its evolution during repeated meshing was simulated using the Archard wear formula. The fatigue damage accumulation of material points on and underneath the contact surface was captured using the Brown-Miller-Morrow multiaxial fatigue criterion. The elastic-plastic constitutive behavior of damaged material points was updated by incorporating the damage variable. Variations in the wear depth and fatigue damage around the pitch point are described, and the effect of surface roughness on the fatigue life is addressed. The results reveal that whether fatigue failure occurs initially on the surface or sub-surface depends on the level of surface roughness. Mild wear on the asperity level alleviates the local stress concentration and leads to a longer surface fatigue life compared with the result without wear.

Keywords: gear contact fatigue; tooth wear; surface roughness; damage accumulation

1 Introduction

Gears are extensively utilized in numerous machines such as helicopters, ships, wind turbines, and vehicles. Particularly in the aviation, gears are important components that influence the reliability of helicopters, aero-engines, vertical-flight vehicles, and other aviation equipments [1]. There is a demand for improved performance, reduced weight, and increased temperature resistance in these aviation applications. Although there are many innovative manufacturing techniques, including surface superfinishing and shot peening that increase the life and reliability of these gears [2], aviation gears can fail or lead to disastrous accidents due to fatigue failures [3]. Gear contact fatigue life is one of the main factors determining the time between overhauls (TBO) of aviation transmissions. The contact fatigue problems of aviation gears are an important bottleneck in the industry. Addressing them requires methods to predict service performance, particularly the fatigue and wear behavior, so that engineers can design anti-fatigue gears to minimize failure rates and maximize reliability. Some typical flank contact failure modes of gears, such as pitting [4], micropitting [5], and deep spalling [6], are shown in Fig. 1. The diversity of contact fatigue failure

* Corresponding author: Huaiju LIU, E-mai: huaijuliu@cqu.edu.cn

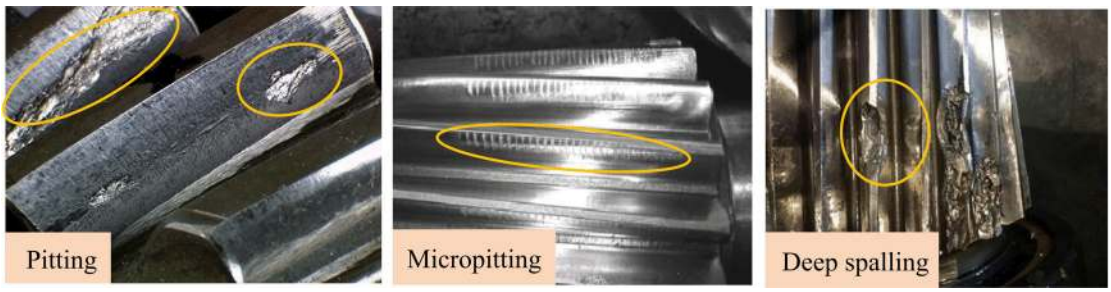

Fig. 1 Some typical flank contact failure modes of gears.

types reflects the complexity of the gear contact fatigue failure mechanism. The mechanism of gear contact fatigue has been the subject of many studies, of which some focused on the fatigue damage and wear process during operation [7–9].

The cyclic loading of machine elements, including gears, bearings, and cams, may progressively result in fatigue fracture after a large number of loading cycles. Among the broad category of fatigue problems, rolling contact fatigue is a special type [10]. Many theoretical and experimental contact fatigue studies have been conducted for over a hundred years. The Hertzian contact theory [11] was approved as the standard reference for the design of tooth surface strength in early times. However, it makes many tribological assumptions for calculating the contact stress field. Thus, it fails when the contribution of surface roughness and other factors is significant. To reveal the failure mechanism and achieve acceptable anti-fatigue performance, Dang Van and Maitournam [12], Brown and Miller [13], and Fatemi and Socie [14], to name a few, proposed multiaxial fatigue criteria based on stress, strain, and critical plane concept. Several excellent reviews describing the intrinsic connections and discrepancies between these criteria can be found in the literature [15, 16]. These fatigue theories are widely used to evaluate fatigue life under complicated multi-axial stress states, such as the repeated contact condition. These original fatigue criteria were extended and modified accordingly to address specific conditions that occur during gear contact. Based on a modified Dang Van diagram, Liu et al. [17] studied the influence of root mean square (RMS) value of surface roughness on the failure risk at critical material points and found that surface roughness significantly increased the contact fatigue failure risk within a shallow area, and the maximum risk appeared near the surface. Qin and Guan [18] predicted the number of loading cycles required for fatigue crack initiation using the Smith-Watson-Topper (SWT) multiaxial fatigue principle [19]. Because fatigue, particularly gear high-cycle fatigue, is a continuous process during which stress and strain change all the time, it is not sufficiently accurate to use the stress result of a single loading moment to predict the entire fatigue life. Based on the definition of a fatigue parameter (FP), a numerical method for calculating the damage caused by repeated rolling contact was proposed by Dang Van [20] and was used to illustrate the applicability of the methodology through a three dimentional (3D) simulation of rolling contact and investigation of rail high-cycle fatigue. Ringsberg et al. [21] combined a multiaxial fatigue crack initiation model with the damage accumulation theory to form a fatigue life prediction strategy for rolling contact fatigue crack initiation. Although this theory considers fatigue failure as a process of damage, it neglects the gradual deterioration of material properties during repeated loading. To address this issue, some scholars have proposed the continuous damage mechanics (CDM), among which the Lemaitre and Chaboche damage-coupled elastic-plastic constitutive formula [22] is widely used. Using the CDM concept, He et al. [23–25] analyzed the effect of residual stress and loading sequence on fatigue damage evolution during gear rolling contact. They pointed out that the influence of the loading sequence on the contact fatigue life gradually decreased as the frequency of load alternations increased. However, the

computational modeling of gear contact failure remains a great challenge, even with advances in computing power and relevant theories.

Different gear manufacturing processes such as hobbing, grinding, and superfinishing yield different surface roughness characteristics of the tooth profile. During repeated gear rolling, the tooth surface micro-topography greatly affects surface-initiated fatigue damage due to stress concentration near the surface. Hannes and Alfredsson [26] developed an asperity point load contact model and demonstrated that asperity height and local asperity friction have the largest effect on crack initiation risk. Suraratchai et al. [27] investigated the influence of machined surface roughness on the fatigue life of aluminum alloy and proposed an approach based on finite element analysis of measured surface topography. The superfinishing manufacturing technique, which remarkably improves the surface micro-topography quality, effectively extends the gear contact fatigue life [28–30].

As the fatigue damage accumulates, the tooth profile also experiences moderate wear under repeated sliding-rolling action. Flodin et al. [31] and Sadeghi et al. [32] simulated the process of gear mild wear based on the well-known Archard wear law. However, analysis of the wear process of any tribological element without considering the surface micro-topography may lead to misleading results. The tooth surface micro-topography gradually changes during repeated rolling-sliding, characterizing wear as a complicated and long process. A dynamic wear evolution model considering surface micro-topography and tribological evolution was established by El-Thalji et al. [33], and their simulated results agree with experimental observations. Yuan et al. [34] proposed a wear reliability investigation of spur gears based on the cross-analysis method of a nonstationary random process that was further verified using test data.

The tooth wear and crack during contact fatigue are not independent of each other. Wear introduces the evolution of surface micro-topography and, perhaps, changes to the general tooth profile if the surface is worn severely. The contact fatigue damage changes the mechanical properties of material points near the surface, while the surface micro-topography gradually evolves under the action of wear and local plastic deformation, thus affecting the evolution of fatigue damage in turn. Quantifying the influence of wear on damage evolution is an intricate matter. Recently, attention has been paid to the coupling mechanism of fatigue and wear during repeated contact. Garcin et al. [35] and Llavori et al. [36] simulated the evolution process of fretting damage by using finite element analysis and analytical calculation, respectively. Based on the CDM theory, Leonard et al. [37], Ghosh et al. [38], and Shen et al. [39] simulated the combined process of fretting wear and fatigue damage and discussed the effects of the surface roughness, frictional coefficient, material hardness, and Young's modulus on fretting wear. Some key results show that wear accelerates the nucleation of fretting fatigue cracks in the partial slip regime and greatly delays crack propagation.

However, studies on the interaction between wear and fatigue damage during gear rolling contact are lacking in the literature. Focusing on the interaction between wear and crack propagation, Fletcher et al. [40] and Mazzù et al. [41] discussed the effect of wear on crack length reduction using computer simulations and experiments, respectively. They considered that the wear could cut off the surface crack and eliminate the small surface crack. The highlight feature of their contribution was the consideration of the coupling mechanism of fatigue behavior and wear evolution. However, the influence of tooth surface micro-topography was not considered, and the effect of wear on pitting and micropitting was not fully explained in their studies. There is great promise for advanced gear design methodology once the fatigue-wear coupling mechanism is discovered.

To describe the interaction between wear and fatigue damage of the gear tooth and to identify failure modes under real tooth surface micro-topography, the elastic-plastic finite element model of an aviation gear pair was established

based on the Archard wear model and the damage-coupled material constitutive behavior. Variations in wear volume and fatigue damage on the near-surface and sub-surface areas around the pitch point area are described, and the effect of surface roughness on fatigue life and failure mode is discussed considering the coupled mechanism of wear damage.

2 Numerical model

To consider the coexisting phenomena of contact fatigue and tooth wear, a finite element model incorporating the measured tooth profile surface roughness was proposed using the commercial software ABAQUS. Figure 2 shows a technical diagram of the simulation process. First, the gear pair was established considering the measured surface roughness and the damage-coupled elastic-plastic constitutive behavior. Second, the surface micro-topography was updated based on the Archard wear model. Then, according to the stress and strain response, the damage rate of material points was calculated based on the Brown–Miller–Morrow multiaxial fatigue criterion and Miner accumulation theory. The fatigue damage of material points was accumulated and the material mechanical properties were updated until the accumulated damage of a certain material point reached the threshold value. Much of the modeling work was conducted with codes incorporating customized algorithms, enabling the accurate prediction of complex damage and wear processes in gear material points.

2.1 Damage-coupled constitutive behavior

Fatigue damage is believed to cause the deterioration of the mechanical properties of the material. Thus, the original elastic-plastic constitutive behavior of a gear material should be updated to consider the time-varying damage. The damage-coupled elastic-plastic constitutive behavior is described with the Lemaitre and Chaboche models [22].

For the elastic-plastic behavior, the yield function f is defined as

$$f = J_2 - \sigma_Y \tag{1}$$

where σ_Y is the initial yield limit of the gear

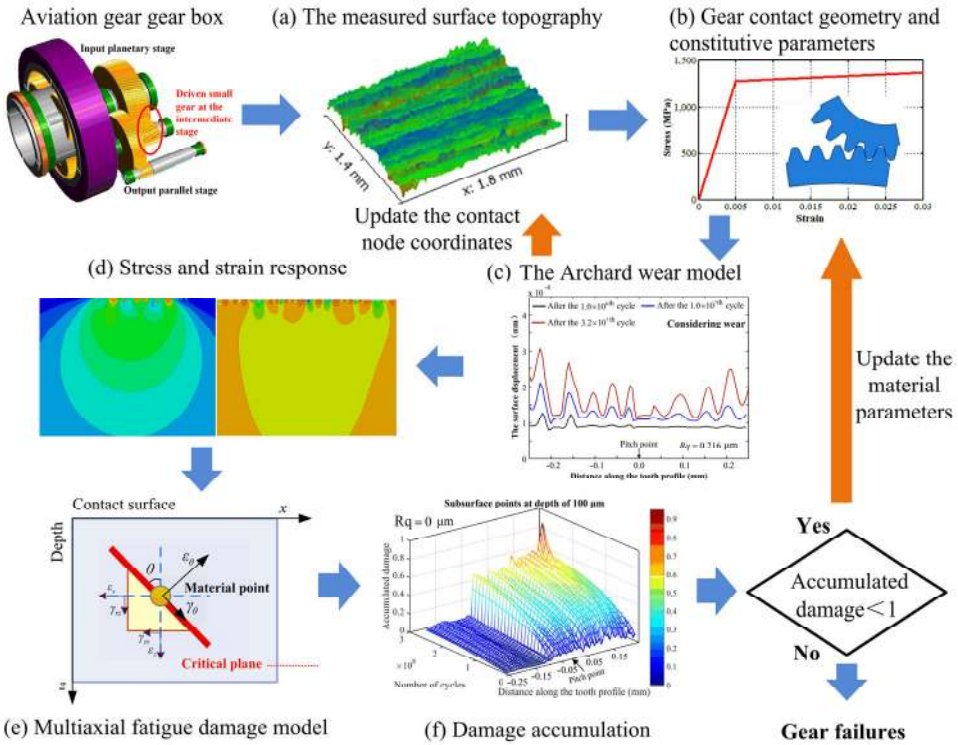

Fig. 2 The technical diagram of the simulation process.

material determined from the initial radius of the yield surface. The symbol J_2 represents the von Mises equivalent stress calculated as

$$J_2 = \left[\frac{3}{2}\left(\frac{\boldsymbol{s}}{1-D}-\boldsymbol{\alpha}\right):\left(\frac{\boldsymbol{s}}{1-D}-\boldsymbol{\alpha}\right)\right]^{\frac{1}{2}} \quad (2)$$

where $\boldsymbol{\alpha}$ is the back-stress tensor representing the center of the yield surface, $\boldsymbol{s}$ is the deviatoric stress tensor, and D is the fatigue damage scalar.

The total strain tensor $\boldsymbol{\varepsilon}$ can be divided into elastic and plastic parts as $\boldsymbol{\varepsilon}=\boldsymbol{\varepsilon}^{\mathrm{e}}+\boldsymbol{\varepsilon}^{\mathrm{p}}$. The stress tensor $\boldsymbol{\sigma}$, which can be calculated from the elastic strain tensor $\boldsymbol{\varepsilon}^{\mathrm{e}}$ and the fatigue damage scalar D, is

$$\boldsymbol{\sigma} = (1-D)C:(\boldsymbol{\varepsilon}-\boldsymbol{\varepsilon}^{\mathrm{p}}) \quad (3)$$

where C represents a material constant. The plastic strain rate $\dot{\boldsymbol{\varepsilon}}^{\mathrm{p}}$ is

$$\dot{\boldsymbol{\varepsilon}}^{\mathrm{p}} = \dot{\lambda}\frac{\partial f}{\partial \boldsymbol{\sigma}} = \frac{3}{2}\dot{\lambda}\frac{\left(\frac{\boldsymbol{s}}{1-D}-\boldsymbol{\alpha}\right)}{J_2(1-D)} \quad (4)$$

where $\partial f/\partial\boldsymbol{\sigma}$ represents the plastic flow direction and $\dot{\lambda}$ is the plastic multiplier, which can be calculated as

$$\dot{\lambda} = \sqrt{\frac{3}{2}\dot{\boldsymbol{\varepsilon}}^{\mathrm{p}}:\dot{\boldsymbol{\varepsilon}}^{\mathrm{p}}} \quad (5)$$

The Prager linear kinematic hardening model [42] was adopted to calculate the back-stress as

$$\dot{\boldsymbol{\alpha}} = \frac{2EM(1-D)}{3(E-M)}\dot{\boldsymbol{\varepsilon}}^{p} \quad (6)$$

where E is the initial Young's modulus. The symbol M, representing the linear kinematic hardening modulus, can be determined from the simple tensile stress-strain curve of the material.

2.2 Fatigue criterion

Before analyzing the fatigue behavior of gear material points using the calculated stress and strain, the response of multi-axial fatigue during gear tooth meshing must be established. There are many multiaxial fatigue criteria in the literature. Among them, the Brown-Miller fatigue criterion [13, 43] concludes that the combined action of shear and normal strain reduces the fatigue life. Therefore, based on combined tension and torsion tests, two strain parameters are required to describe the fatigue process. Meanwhile, large mean stress exists underneath the contact surface. The mean stress effect is included using Morrow's modified approach by subtracting the mean stress σ_{m} from the fatigue strength coefficient σ_{f}'. The Brown–Miller–Morrow fatigue life model [44] coupled with fatigue damage is expressed as

$$\frac{\Delta\gamma_{\max}}{2}+S\Delta\varepsilon_{\mathrm{n}} = A\frac{(\sigma_{\mathrm{f}}'-\sigma_{\mathrm{m}})}{E(1-D)}(2N_f)^b + B\varepsilon_f'(2N_f)^c \quad (7)$$

where $\Delta\gamma_{\max}$ and $\Delta\varepsilon_{\mathrm{n}}$ are the maximum shear strain amplitude and normal strain amplitude on the critical plane, respectively. σ_{m} represents the mean stress on the critical plane. b and c denote the fatigue strength exponent and fatigue ductile exponent, respectively. σ_{f}' and $\varepsilon_{\mathrm{f}}'$ represent the fatigue strength coefficient and fatigue ductile coefficient, respectively. The parameter S, as a material constant, can be determined through classical torsion and push-pull experiments. The other two material constants are calculated as $A=1.3+0.7S$ and B=1.5+0.5S, respectively. $2N_{\mathrm{f}}$, as an intermediate variable, represents the fatigue life of each material point according to the gear rolling contact.

According to the selected fatigue criterion, the critical plane is the plane with the maximum shear strain. Figure 3 demonstrates the definition of the critical plane at a material point and the distribution of the maximum shear strain of the selected gear. The angle θ from the vertical direction, as the angle of the critical plane, is illustrated in Fig. 3.

Because the critical plane of each material point is unknown, the shear strain, normal strain, and normal stress must be calculated at each candidate plane of every material point of interest in advance. In terms of the stress transformation theory [45], the normal stress σ_θ, normal strain ε_θ, and shear strain γ_θ on each plane with a specified angle can be expressed as

$$\begin{cases}\sigma_\theta = \sigma_x\cos^2\theta+\sigma_z\sin^2\theta+2\tau_{xz}\sin\theta\cos\theta\\ \varepsilon_\theta = \varepsilon_x\cos^2\theta+\varepsilon_z\sin^2\theta+\gamma_{xz}\sin\theta\cos\theta\\ \gamma_\theta = \gamma_{xz}(\cos^2\theta-\sin^2\theta)+2(\varepsilon_z-\varepsilon_x)\sin\theta\cos\theta\end{cases} \quad (8)$$

where σ_x, σ_z, and τ_{xz} represent the two normal stresses and the shear stress, respectively. ε_x, ε_z,

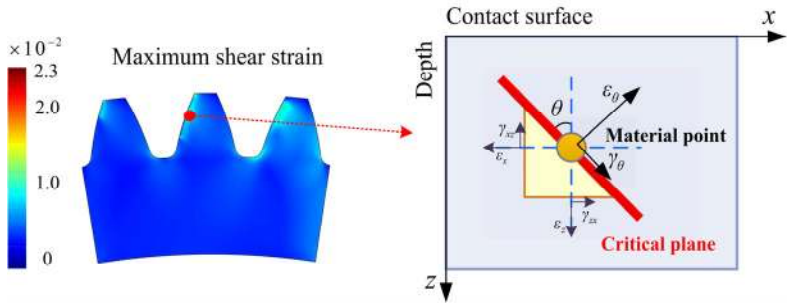

Fig. 3 The definition of the critical plane.

and γ_{xz} represent the two normal strains and the shear strain, respectively. σ_θ, ε_θ, and γ_θ are the normal stress, normal strain, and shear strain on the plane with the angle θ from the rolling direction, respectively.

On the critical plane, the main parameters of the maximum shear strain amplitude $\Delta\gamma_{\max}$, normal strain amplitude $\Delta\varepsilon_{\mathrm{n}}$, and mean normal stress σ_{m} can be calculated as

$$\begin{cases} \Delta\gamma_{\max} = \dfrac{\gamma_{\max} - \gamma_{\min}}{2} \\ \Delta\varepsilon_{\mathrm{n}} = \dfrac{\varepsilon_{\max} - \varepsilon_{\min}}{2} \\ \sigma_{\mathrm{m}} = \dfrac{\sigma_{\max} + \sigma_{\min}}{2} \end{cases} \tag{9}$$

where $\gamma_{\max}$ and $\gamma_{\min}$ represent the maximum and minimum shear strain on the critical plane, respectively. $\varepsilon_{\max}$ and $\varepsilon_{\min}$ represent the maximum normal strain and maximum normal stress on the critical plane, respectively. $\sigma_{\max}$ and $\sigma_{\min}$ are the minimum normal strain and minimum normal stress on the critical plane, respectively.

When considering the surface micro-topography and its evolution, the stress field near the surface constantly changes. It is not accurate to estimate the gear fatigue life based on the stress-strain results of a single rolling contact cycle. Therefore, the Brown–Miller–Morrow multiaxial fatigue criterion and Miner accumulation theory were combined to calculate the fatigue life in this study. The intermediate variable $2N_{\mathrm{f}}$ of each material point can be acquired using Eqs. (7)–(9), and then the damage rate of this contact case can be calculated.

According to the Miner accumulation theory [46], which is one of the most widely accepted fatigue cumulative damage theories, the single damage rate is

$$\frac{\mathrm{d}D}{\mathrm{d}N} = \frac{1}{2N_{\mathrm{f}}} \tag{10}$$

Because carburized gears usually endure 1×10^7–1×10^{10} loading cycles before final failure, this kind of fatigue is characterized by a high cycle fatigue (HCF) region or even the ultra-high cycle fatigue (UHCF) region. Solving the aforementioned damage-coupled constitutive equations requires a large amount of time and great computing ability for each loading cycle. To solve this computational cost problem, the "jump-in cycle" method, employed by many other scholars [25, 47, 48], was applied in this work. This jump-in cycle framework allows relatively easy modeling of the HCF and UHCF damage evolution. With such a simplified and straightforward method, a loading block represents a finite number of cycles ΔN over which the stress and strain fields are assumed to be unchanged. The updated damage variable after each loading block is given as

$$D_j^{i+1} = D_j^i + \left(\frac{\mathrm{d}D}{\mathrm{d}N}\right)_j^i \times \Delta N \tag{11}$$

The degradation of material mechanical properties after each loading block is

$$E_j^{i+1} = E_j^i(1-D_j^i),\ M_j^{i+1} = M_j^i(1-D_j^i),\ (\sigma_Y)_j^{i+1} = (\sigma_Y)_j^i(1-D_j^i) \tag{12}$$

where i represents the current loading block and j indicates the label of the material point. Different interval values of ΔN were selected for different loading conditions. For some cases where the root mean square (RMS) value of the surface roughness Rq is large, the surface micro-topography changes greatly within the very early

operating stage, so the chosen ΔN should be small enough to describe the evolution tendency of damage. The principle of the "jump-in cycle" method is shown in Fig. 4. In this work, the threshold value of $D_c = 0.95$ was defined to indicate material failure.

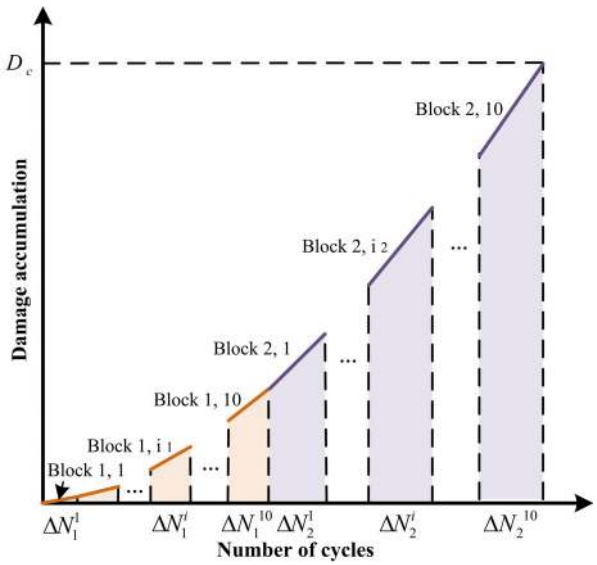

Fig. 4 The principle of the "jump-in cycle" method.

2.3 Initial surface roughness and the Archard wear model

Real tooth surface micro-topography was considered through direct measurement with an optical profilometer. The surface micro-topography of the selected gear tooth was measured using a white light interferometer assembled on a commercial Rtec multifunction tribology tester MFT-5000. This profilometer is a precision optical instrument with analysis functions for various surface forms and roughness parameters. Figure 5 illustrates that the measuring length of the surface micro-topography was 1.37 mm along the tooth profile direction. The RMS value of the initial surface roughness Rq was calculated to be 0.216 μm, representing a typical as-ground surface state.

To describe the evolution process of surface micro-topography during repeated gear contact, the Archard wear model [49], which is a simple and efficient model describing sliding wear based on the theory of asperity contact, was adopted in this study. The wear depth Δh per loading cycle can be expressed as

$$\Delta h = \Delta N \times k \int p \mathrm{d}s \Delta h = \Delta N \times k \int p \mathrm{d}s \tag{13}$$

where p represents the contact pressure at each time increment, $\mathrm{d}s$ represents the incremental slip distance, and k stands for the wear coefficient, which relates to the material properties such as the hardness.

The wear simulation methodology is based on the Archard wear model implemented with an adaptive meshing technique and the subroutine UMESHMOTION. The subroutine UMESHMOTION provided by the commercial software ABAQUS was adopted to extract the contact pressure p, increment of slip distance $\mathrm{d}s$, and coordinates of the current contact node at the current moment, from which the wear depth was calculated accordingly. Once the wear depth per loading cycle was determined, the coordinates of the surface contact node were updated.

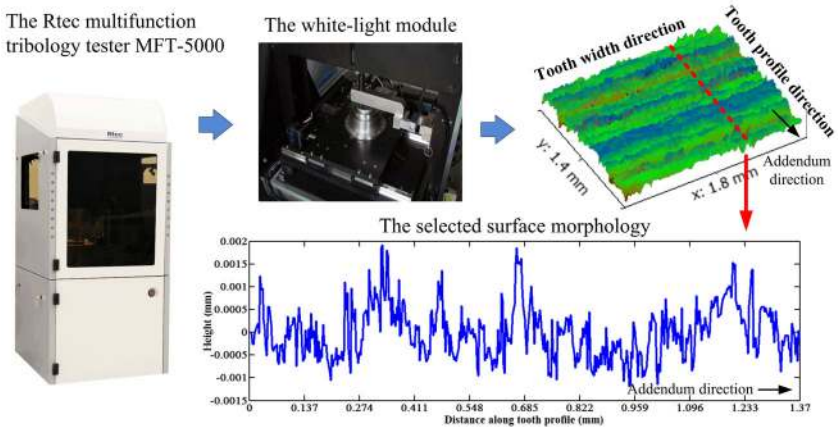

Fig. 5 Measuring of tooth surface roughness.

A general programming diagram of this numerical work is shown in Fig. 6. According to the material parameters from the fatigue study [50] and wear study [51] using the same or similar steels, the required fatigue parameters and wear parameters are listed in Table 1.

2.4 The finite element contact model

A pair of aviation gears used in a helicopter was selected as the sample. The gear material was AISI 9310 [52], and its chemical composition is listed in Table 2. The geometric parameters and working conditions of the gear pair are listed in Table 3. The initial Young's modulus of the gear teeth in conjunction is E=210,000 MPa, which decreased monotonically as the damage accumulated. Figure 7 shows that the contact of the gear pair was established in ABAQUS. The pitch radii of the two gears were 64.135 and 37.465 mm, respectively. The friction coefficient was 0.1, which conforms to engineering practice. Because the pinion often suffers from contact-fatigue induced failure in practical applications, attention was paid to its wear response and fatigue damage. The surface

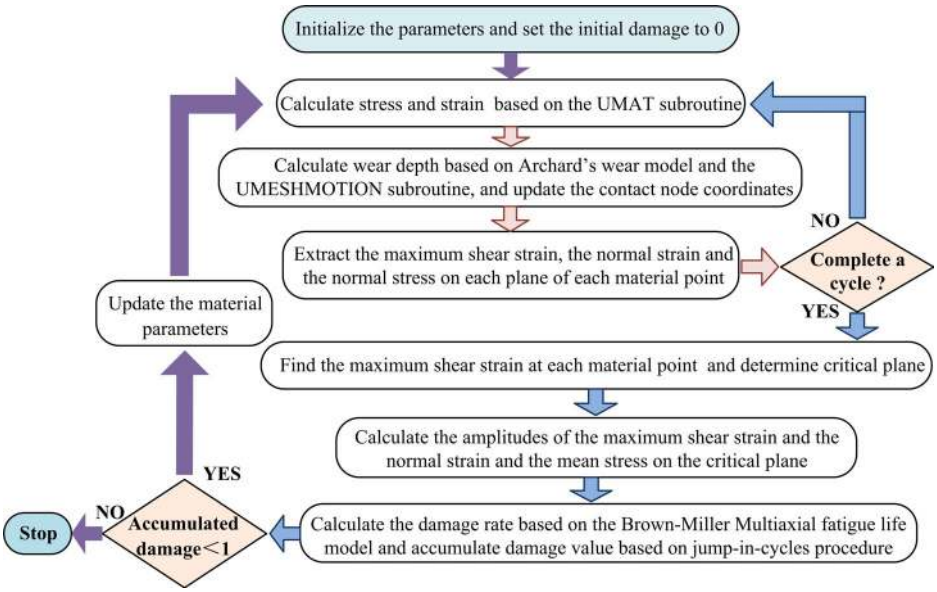

Fig. 6 Programming diagram of simulation.

Table 1 Fatigue and wear parameters of the material.

Contact fatigue parameters							Wear parameter
σ_f' (MPa)	ε_f'	b	c	S	A	B	k (MPa^{-1})
2894	0.134	–0.087	–0.58	0.5	1.65	1.75	2.0×10^{-11}

Table 2 The chemical composition of AISI 9310.

C	Mn	Si	Ni	Cr	Mo	Cu	P	S	Al	Co
0.12	0.57	0.27	3.33	1.29	0.11	0.11	0.006	<0.001	0.05	0.011

Table 3 Gear geometry, working conditions of the gear.

Parameters	Values	Parameters	Values
Teeth number Z_1 / Z_2	101/59	The pressure angle	20°
Tooth normal module m_n	1.27	Tooth width of pinion G (mm)	7.65
Initial Young's modulus E (MPa)	2.1×10^5	The Poisson's ratio ν	0.3
Initial yield limit σ_Y (MPa)	1,300	Hardening modulus M (GPa)	10.5
Wheel speed N_1 (r/min)	77	Nominal output torque T_1 (N·mm)	1.2×10^5

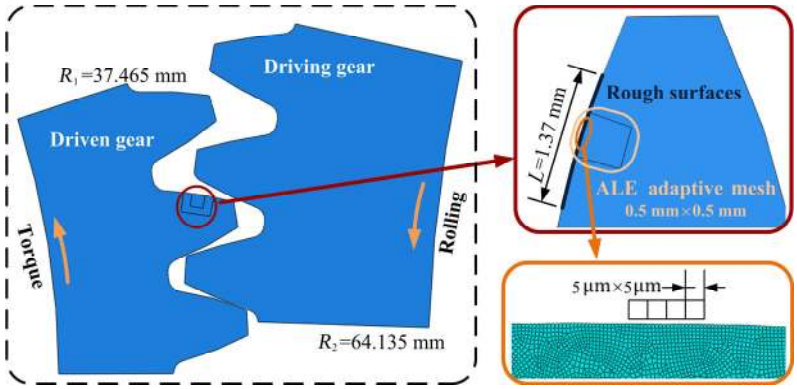

Fig. 7 Gear contact model with rough surface.

micro-topography mentioned above was attached to the tooth surface near the pitch point of the pinion in ABAQUS. As spur gears, the plane strain condition was assumed to reduce the contact into a two-dimensional problem and reduce the calculation cost. A straightforward 3D extension of the proposed model can be readily realized if needed in the future. A 0.5 mm square area near the pitch point is selected to use the ALE adaptive mesh technique to calculate wear. In the contact area, a fine mesh grid size of 5 μm × 5 μm was enough to provide converged results with acceptable computational time.

3 Results and discussion

3.1 Evolution of surface micro-topography and damage

First, the general contact pressure distribution and von Mises stress near the pitch point for the smooth surface case are discussed. Two different systems, one considering wear and the other not, are examined and compared with each other. Figure 8 shows the distribution of contact pressure, surface normal displacement (red lines), and von Mises stress at three selected stages for the smooth surface case under an output torque condition of 120 N·m. The black lines, including black solid, black dashed, and black dotted lines, show the distribution of contact pressure at three contact moments. Because the operating stage of $1.0\times10^{7\text{th}}$ cycle (as shown in Fig. 8(a)) represents the first loading block, wear has not yet contributed to the situation. The Hertzian half contact width under this condition was approximately 0.16 mm, while the Hertzian maximum contact pressure P_H was approximately 1,000 MPa.

The permanent surface displacement perpendicular to the tooth surface results from wear and plastic

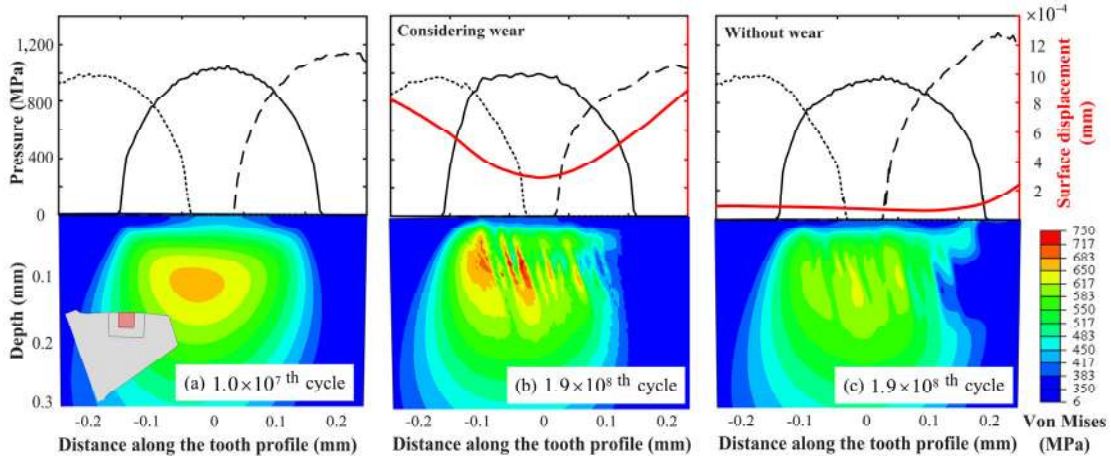

Fig. 8 Pressure, surface displacement, and stress at smooth surface: (a) $1.0\times10^{7\text{th}}$ cycle, (b) $1.9\times10^{8\text{th}}$ cycle considering wear, and (c) $1.9\times10^{8\text{th}}$ cycle without wear.

deformation under repeated loading. Compared with the result of the first loading block, Fig. 8(b) represents the result after 1.9×10^8 cycles. It shows that the maximum contact pressure did not change much when wear was considered, but the distribution shape of the contact pressure changed slightly due to the variation of the tooth profile under the permanent normal displacement. Compared with the no-wear case (Fig. 8(c)), the surface normal displacement became larger when tooth wear was considered. The largest amount of wear occurred far from the pitch point, which was also demonstrated in Ref. [53]. Figure 8(c) shows that even though the wear was not considered, a non-zero normal displacement occurred because of the surface plastic deformation, but the magnitude was primarily below 0.2 μm.

The maximum value of the von Mises stress considering wear was approximately 750 MPa, and when the wear effect was excluded, it was reduced to approximately 640 MPa. Meanwhile, because the damage accumulated non-uniformly inside the solid, the stress distribution displayed local fluctuations inside the solid during the subsequent stages of operation. Once the tooth wear was taken into consideration, the stress fluctuation became more evident.

The surface normal displacement was further studied, particularly focusing on the influence of wear. Figure 9 illustrates the surface displacement curve for the case with an initial Rq value of 0.216 μm. The result of Fig. 9(a) considers wear, whereas Fig. 9(b) does not. Surface normal displacement is caused by wear and plastic deformation along the vertical direction of the contact surface. Whether wear was considered or not, the peak normal displacement always increased as the loading cycle increased. This conclusion is confirmed in Ref. [54]. At an early operating stage (represented by the black lines), the surface displacements with and without wear are similar. As the cycle number increased to 1.0×10^7, there is a clear difference between the blue curves in the two sub-figures. The high contact pressure at the peaks leads to a large wear depth at the peak, similar to the finding in Ref. [55]. As the loading cycle increased further, the differences between the two results (with and without wear) become more significant. The wear depth increased for points farther away from the pitch point along the line of action. Wear can occur not only in surface asperities but also in valleys, particularly in areas far away from the pitch point.

Figure 10 indicates the evolution of the surface micro-topography after different loading cycles with an initial Rq of 0.216 μm. Figure 10(a) considers wear while Fig. 10(b) does not. It should be noticed that once the general tooth profile was considered, the base line of the surface profile is not a straight line but a radius of curvature. Results show that as the wear proceeded, the height difference between the peak and the valley declined, and the surface micro-topography tended to be flat [55, 56]. This is mainly because

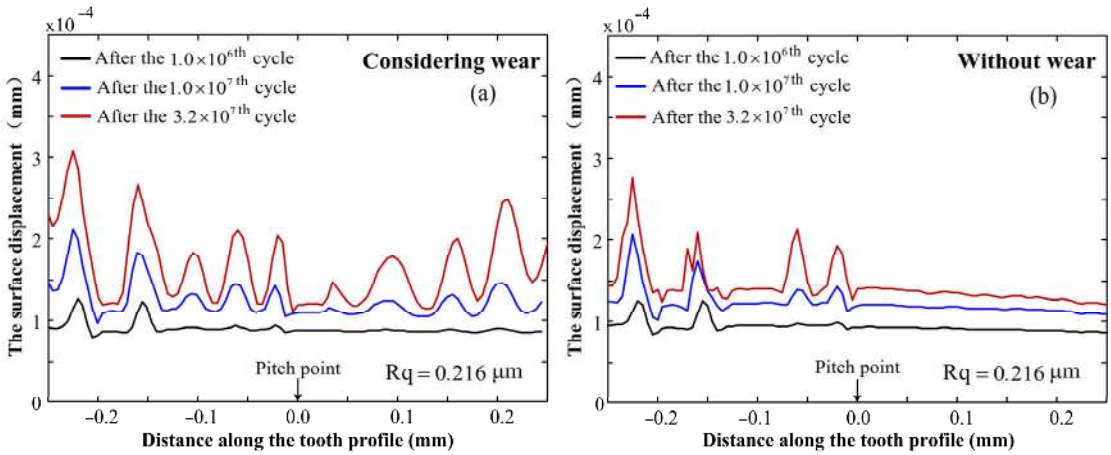

Fig. 9 Comparison of surface displacement with and without wear.

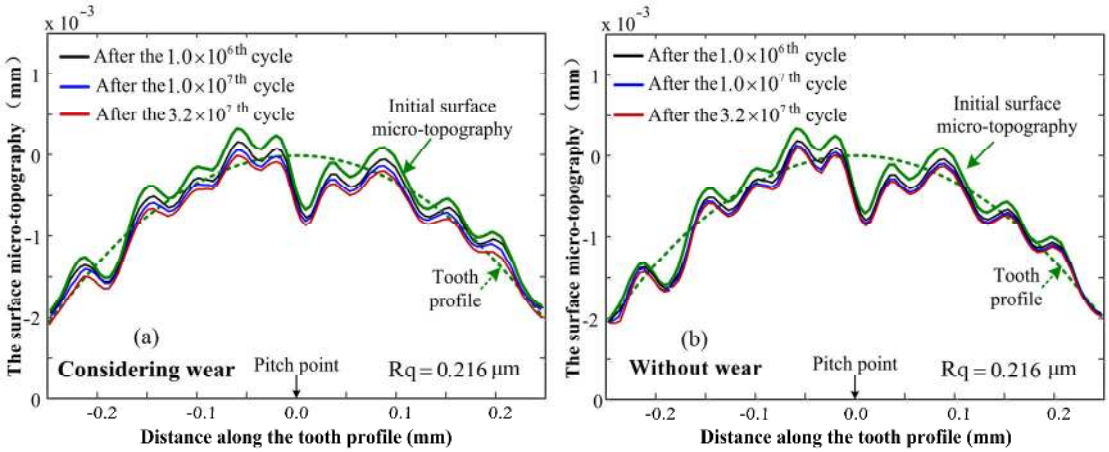

Fig. 10 Comparison of surface micro-topography with and without wear.

the wear depths at roughness peaks are larger than those at valleys during the loading cycles.

The normal strain amplitude $\Delta\varepsilon_n$ and the shear strain amplitude $\Delta\gamma_{max}$ are the two governing parameters in the Brown–Miller–Morrow fatigue criterion and should be calculated from the time-varying stress-strain response. Figure 11 displays the two parameters at different operating stages for the case of initial surface roughness Rq of 0.216 μm. Both the near-surface and subsurface areas are of concern. In addition to the large amplitudes at the Hertzian contact subsurface area, large amplitudes also appear locally near the surface due to surface micro-topography. The amplitudes of the normal strain $\Delta\varepsilon_n$ and shear strain $\Delta\gamma_{max}$ in the near-surface area fluctuate remarkably due to the coexistence of asperities and valleys. The amplitudes of the normal strain of most material points are less than the shear strain amplitudes, as confirmed by the results of Ref. [54]. It is readily observed that as the loading cycle number increased, the amplitudes of the normal strain $\Delta\varepsilon_n$ and shear strain $\Delta\gamma_{max}$ in the subsurface gradually increased. This is a consequence of damage accumulation that leads to a reduced Young's modulus and increased strain.

The damage rate at each loading block is determined based on the summation of the amplitudes of the shear strain and normal strain. Figure 12 shows the relationships between the damage rate and the strain amplitude summation at different operating stages. According to the

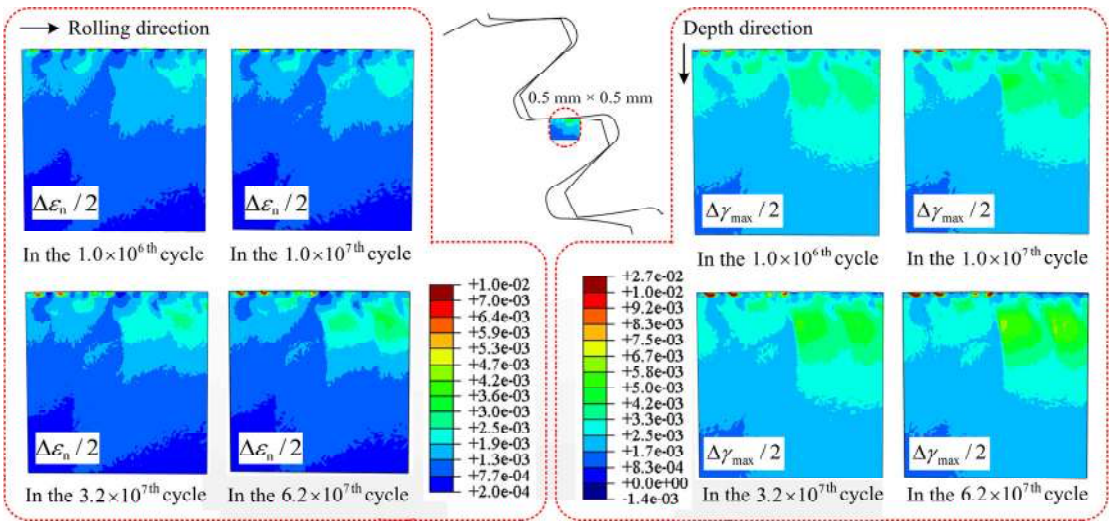

Fig. 11 Amplitudes of normal strain and shear strain at different number of cycles.

Brown–Miller–Morrow multiaxial fatigue criterion, fitted curves are depicted in this figure when zero mean stress was assumed. To distinguish the degree of material damage, envelope curves with different Young's modulus were adopted. The black, green, orange, and purple curves represent the cases where $E = 210$, 105, 84, and 21 GPa, respectively. The dotted black line represents Young's modulus of $E = 210$ GPa and mean stress of −1,000 MPa. To further analyze the damage performance near the surface and subsurface, material points at a depth of 0.1 mm (red scatter) and at a depth of 5 μm (blue scatter) were selected to analyze the relationship between the summation of strain amplitudes and the damage rate under different loading cycles. For comparison, Fig. 12(d) depicts the situation without wear.

The results after 2.0×10^5 cycles (the first loading block) are shown in Fig. 12(a). Before this first loading block, there was no damage at the material points, and Young's modulus for all material points was $E = 210$ GPa. This sub-figure shows that the material point with the maximum damage rate occurred at near-surface asperity, with a magnitude less than 8.0×10^{-8}. The summation of strain amplitudes $\Delta\varepsilon_n + \Delta\gamma_{max}$ in the subsurface lies in the region of 0.003–0.006, and the maximum damage rate at this subsurface area was less than 3.0×10^{-8}. Due to the role of surface micro-topography, the strain amplitude-damage rate of near-surface material points displays a scatter distribution.

Figure 12(b) shows the damage rate as the number of cycles reached 3.2×10^7. The material point with the maximum damage rate occurred in the subsurface, with magnitudes below 1.0×10^{-8}. Moreover, the material points at the subsurface are

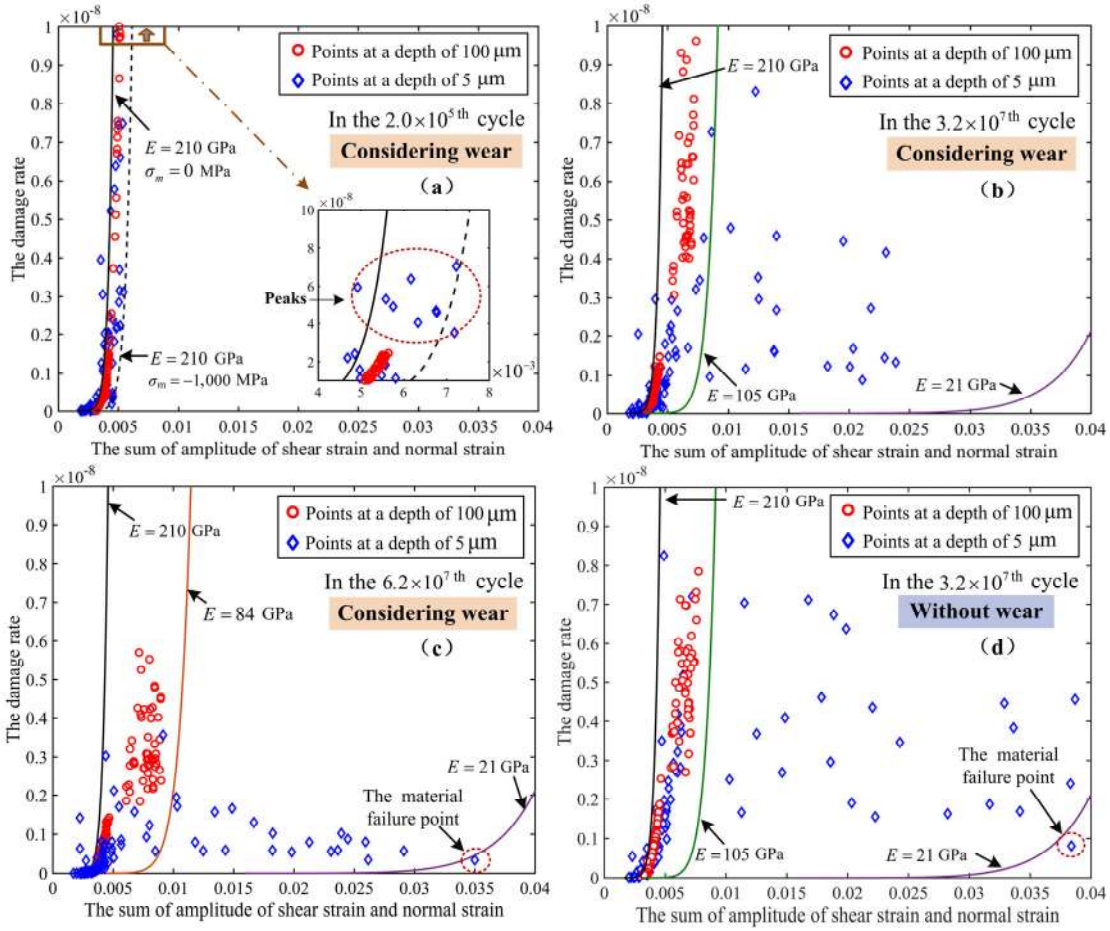

Fig. 12 Relationships between the damage rate and sum of strain amplitudes.

more dispersed than those illustrated in Fig. 12(a), which is caused by the varying degree of damage degree for different material points. However, the scatters are mostly located between the black line (E = 210 GPa) and the green line (E = 105 GPa). The scatters near the surface were more dispersed, which is caused by the reduction of material properties and surface micro-topography.

The damage rate at the loading cycle of $6.2\times10^{7\text{th}}$ is shown in Fig. 12(c). The damage rates of material points near the surface and subsurface continued to decrease. The maximum strain amplitude of material points in the subsurface was less than 0.01, and the maximum damage rate was below 0.6×10^{-8}. The black line (E = 210 GPa) and the orange line (E = 84 GPa) became the new envelope for the material points in the subsurface. There is a blue point outside the purple curve (E = 21 GPa). This material point is considered as the first one to fail.

Figure 12(d) shows the damage rate at the loading cycle of $3.2\times10^{7\text{th}}$ without considering wear. Compared with the results considering wear (Fig. 12(b)), the material points near the surface were more dispersed and the damage rate in the subsurface was slightly lower. A blue scatter outside the purple curve (E = 21 GPa) is anticipated to be the first failed material point. A comparison of the results between Figs. 12(b) and 12(d) reveals that wear smooths the original rough surface, reducing the strain amplitude of some rough peaks and retarding the appearance of pitting.

In summary, with the increase in the loading cycles, the summation of the amplitudes of the normal strain and shear strain $\Delta\varepsilon_{\text{n}}+\Delta\gamma_{\max}$ of the damaged material point increased gradually, and the growth degree depended on the degree of damage at this material point. But the damage rate decreased gradually, which is consistent with the fitted curves based on the Brown–Miller–Morrow multiaxial fatigue criterion.

Figure 13 displays the damage distribution at different stages by setting the low threshold damage to 0.1 so that material points with negligibly small damage are not visible. As shown in the figure, the distribution pattern of the accumulated damage changes at different stages. At the loading cycle of 1.0×10^{6}, the maximum damage appears near the surface and its magnitude reaches 0.392, while the damage at subsurface is below 0.1. It is readily observed that as the loading cycle number increased, the number of material points with damage above 0.1 gradually increased. At the loading cycle of 6.2×10^{7}, the maximum damage reached 0.95 in the near-surface area, indicating the first failed material point. Meanwhile, the maximum damage at the subsurface area was only approximately 0.5, indicating a longer fatigue life compared with near-surface points. Thus, it is concluded that

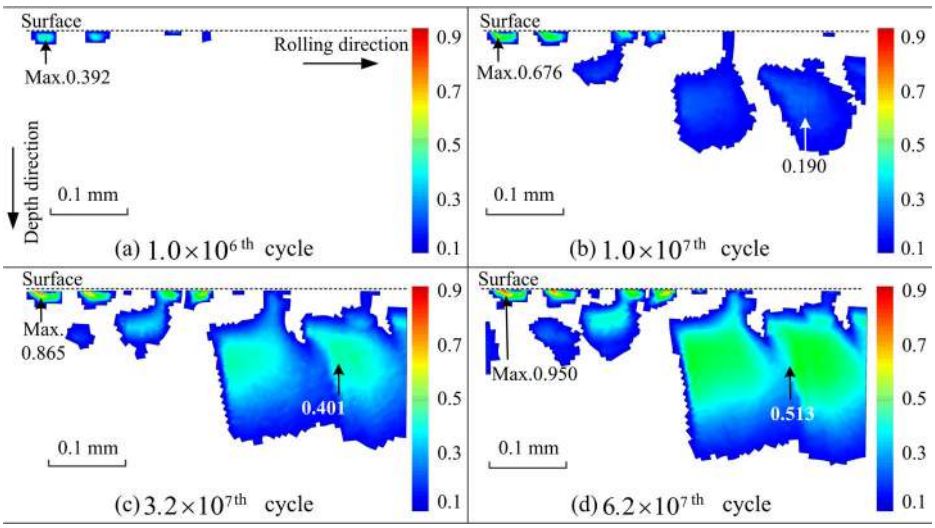

Fig. 13 Distribution of the accumulated damage in different cycles.

under the case with Rq of 0.216 μm, surface-initiated fatigue failure will occur. It is worth noting that the failure type (whether surface-initiated or subsurface-initiated failure) depends on the level of surface roughness. For this purpose, the influence of the root mean square value of surface roughness Rq on the damage accumulation and failure type is discussed in the following section.

3.2 Effect of the RMS value of surface roughness

The effects of surface roughness on the coupled evolution of damage and wear are a primary concern in this work. The evolution for a specific case with Rq of 0.216 μm is first discussed, as shown in Fig. 14. The smooth surface result is also depicted in Fig. 14(d) for comparison. Figures 14(a) and 14(b) represent the near-surface and subsurface areas, respectively. The material points at depths of 5 and 100 μm were selected to represent near-surface and subsurface results, respectively. For near-surface asperity material points (indicated as Points A and B for instance), the damage accumulated rapidly in the early stage and slowed down as the damage accumulated to a considerable amount. With respect to the subsurface area, as shown in Fig. 14(b), the damage accumulated more smoothly compared with the near-surface damage. The damage accumulation of subsurface material points grew faster at low cycle numbers. The damage accumulation gradually slowed down as the loading cycles continued, as shown in Fig. 14(c), while maintaining a considerable accumulation rate. The tendency of damage accumulation in the subsurface was consistent with that reported in Ref. [57].

For comparison, the process of damage accumulation for the smooth surface case is illustrated in Fig. 14(c). It can be observed that for subsurface material points, the damage accumulated smoothly as the loading cycles increased. In the very late stage, one of the most dangerous subsurface points, indicated as Point E, rapidly accumulated damage from 0.6 up to the failure threshold value. This damage acceleration

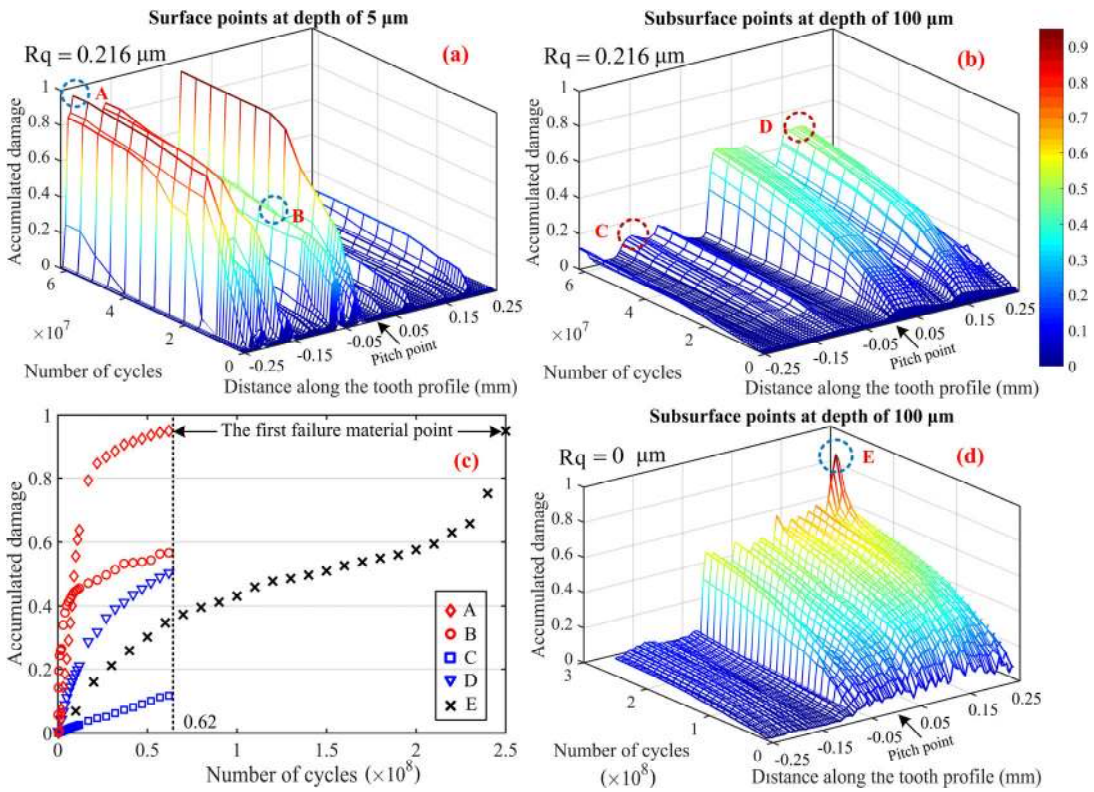

Fig. 14 Evolution of damage with RMS of 0.216 μm.

phenomenon has also been observed in many other studies applying the continuous damage theory [58–60]. For the rough surface case, the maximum damage at the subsurface area was limited to approximately 0.5, as the first near-surface point failed, indicating the surface-initiated failure mode.

The damage distribution with different surface roughness conditions is shown in Fig. 15. For comparison, cases without wear effect are provided in the lower line. The first failed point occurred in the subsurface Rq below 0.2 μm, while it occurred near the surface when Rq exceeded 0.2 μm. Compared with the cases without the wear effect, the contact fatigue life was slightly higher when the wear effect was considered, regardless of the surface roughness. One explanation is that wear alleviates the asperity heights and changes the tooth profile, leading to a reduction in stress concentration and improvement in fatigue life.

Figure 16 statistically shows the fatigue life and failure mode under various surface roughness conditions. It shows that the contact fatigue life decreased as the surface roughness rose, particularly when a critical level of roughness was exceeded. When the surface roughness Rq was less than 0.2 μm, the gear contact fatigue life was very high, and the failure occurred in the subsurface area. Townsend et al. [61, 62] conducted many fatigue experiments on the AISI 9310 gear under the surface condition with surface roughness less than 0.2 μm. The results showed that the failure mode of most specimens was pitting and the probability of the fatigue life exceeding 1×10^8 cycles was greater than 80%. Under the given condition, when the surface roughness Rq exceeded 0.2 μm, the failure tended to occur near the surface, indicating a surface-initiated failure. As the surface roughness increased, a similar transition from sub-surface initiated failure to surface-initiated failure was also observed in Ref. [63]. Currently, the fine level of surface finishing with Rq below 0.2 μm can be achieved using a

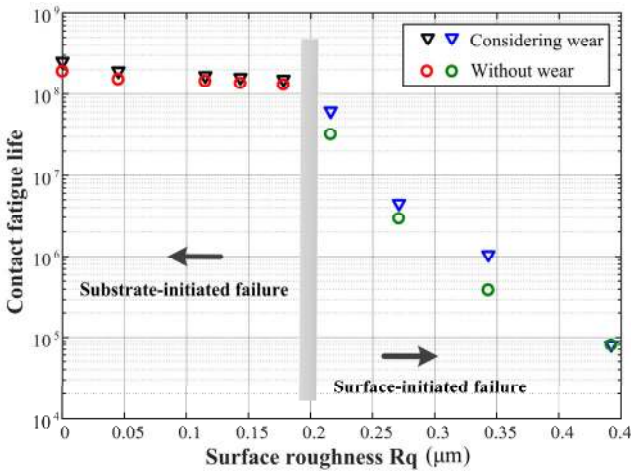

Fig. 16 Contact fatigue life under different surface roughness Rq.

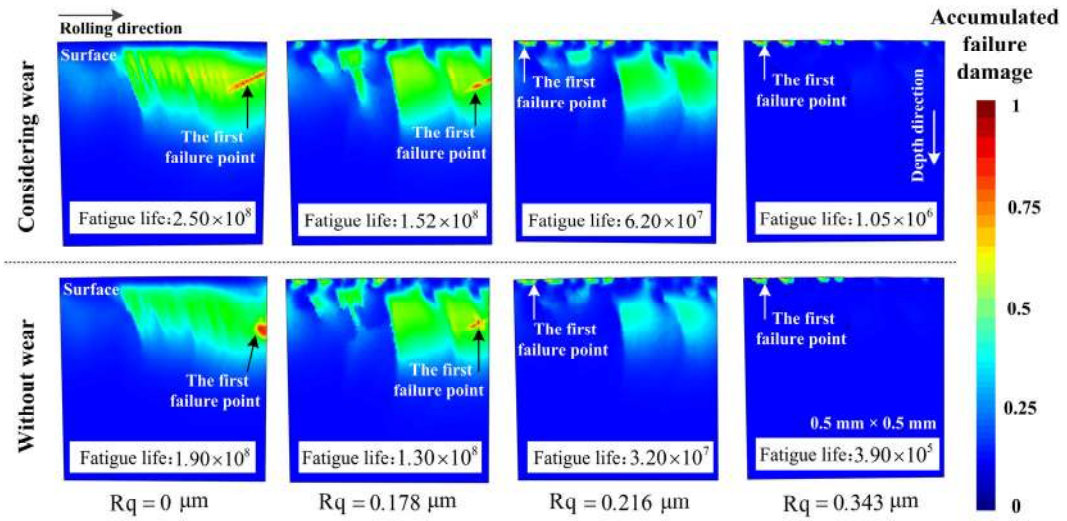

Fig. 15 Effect of surface roughness on damage with and without wear.

superfinishing technique, which will significantly benefit the contact fatigue performance. Nevertheless, the role of tooth surface roughness requires further investigation, particularly in the case with lubrication.

4 Conclusions

To solve the complicated coupling effect of fatigue damage and tooth wear during high-cycle gear meshing, a finite element contact model pair that considered surface roughness, wear evolution, damage accumulation, and modulus deterioration was developed for an aviation gear. The numerical findings were compared with existing literature results. The conclusions can be summarized as follows:

1) Once tooth wear was considered, the minimum surface normal displacement of the tooth profile appeared near the pitch point due to the nearly pure rolling condition at that point. The wear depth increased for points farther away from the pitch point along the tooth profile.

2) Damage to near-surface material points at some asperities accumulated rapidly in the early stage. As the wear proceeded, their damage accumulation slowed. The damage to the sub-surface material points accumulated smoothly as the number of loading cycles increased.

3) Sub-surface material points will quickly fail if the accumulated damage exceeds 0.6 and the material point is still in the stress concentration region.

4) Under the given condition, subsurface-initiated contact fatigue failure occurs when the surface roughness Rq is below a critical level, while surface-initiated failure appears as the surface roughness exceeds this value.

Acknowledgements

The work was supported by the National Key R&D Program of China (Grant No. 2018YFB2001300).

References

[1] Link H, LaCava W, Van Dam J, McNiff B, Sheng S, Wallen R, McDade M, Lambert S, Butterfield S, Oyague F. *Gearbox Reliability Collaborative Project Report: Findings from Phase 1 and Phase 2 Testing*. Golden (United States): National Renewable Energy Lab, 2011.

[2] Krantz T, Anderson C, Shareef I, Fetty J. Testing aerospace gears for bending fatigue, pitting, and scuffing. In *Proceedings of the ASME 2017 International Design Engineering Technical Conferences & Computers and Information in Engineering Conference*, Cleveland, Ohio, USA, 2017

[3] Nygaard J R, Rawson M, Danson P, Bhadeshia H K D H. Bearing steel microstructures after aircraft gas turbine engine service. *Mater Sci Technol* **30**(15): 1911–1918 (2014)

[4] Glodež S, Winter H, Stüwe H P. A fracture mechanics model for the wear of gear flanks by pitting. *Wear* **208**(1–2): 177–183 (1997)

[5] Al-Tubi I S, Long H, Zhang J, Shaw B. Experimental and analytical study of gear micropitting initiation and propagation under varying loading conditions. *Wear* **328–329**: 8–16 (2015)

[6] Chaari F, Baccar W, Abbes M S, Haddar M. Effect of spalling or tooth breakage on gearmesh stiffness and dynamic response of a one-stage spur gear transmission. *Eur J Mech A/Solids* **27**(4): 691–705 (2008)

[7] Zhong W, Hu J J, Shen P, Wang C Y, Lius Q Y. Experimental investigation between rolling contact fatigue and wear of

high-speed and heavy-haul railway and selection of rail material. *Wear* **271**(9–10): 2485–2493 (2011)

[8] Morales-Espejel G E, Rycerz P, Kadiric A. Prediction of micropitting damage in gear teeth contacts considering the concurrent effects of surface fatigue and mild wear. *Wear* **398–399**: 99–115 (2017)

[9] Chernets M. A method for predicting contact strength and life of archimedes and involute worm gears, considering the effect of wear and teeth correction. *Tribol Ind* **41**(1): 134–141 (2019)

[10] Sadeghi F, Jalalahmadi B, Slack T S, Raje N, Arakere N K. A review of rolling contact fatigue. *J Tribol* **131**(4): 041403 (2009)

[11] Hertz H. UBer die Berührung fester elastischer Körper. *J Reine Angew Math* **92**: 156–171 (1882)

[12] Van K D, Maitournam M H. Steady-state flow in classical elastoplasticity: Applications to repeated rolling and sliding contact. *J Mech Phys Solids* **41**(11): 1691–1710 (1993)

[13] Brown M W, Miller K J. A theory for fatigue failure under multiaxial stress-strain conditions. *Proce Inst Mech Eng* **187**(1): 745–755 (1973)

[14] Fatemi A, Socie D F. A critical plane approach to multiaxial fatigue damage including out-of-phase loading. *Fatigue Fract Eng Mater Struct* **11**(3): 149–165 (1988)

[15] You B R, Lee S B. A critical review on multiaxial fatigue assessments of metals. *Int J Fatigue* **18**(4): 235–244 (1996)

[16] Karolczuk A, Macha E. A review of critical plane orientations in multiaxial fatigue failure criteria of metallic materials. *Int J Fract* **134**(3–4): 267–304 (2005)

[17] Liu H L, Liu H J, Zhu C C, Sun Z D, Bai H Y. Study on contact fatigue of a wind turbine gear pair considering surface roughness. *Friction* **8**(3): 553–567 (2020)

[18] Qin W J, Guan C Y. An investigation of contact stresses and crack initiation in spur gears based on finite element dynamics analysis. *Int J Mech Sci* **83**: 96–103 (2014)

[19] Smith R N, Watson P, Topper T H. A stress-strain parameter for the fatigue of metals. *J Mater* **5**(4): 767–778 (1970)

[20] Van K D, Maitournam M H. On some recent trends in modelling of contact fatigue and wear in rail. *Wear* **253**(1–2): 219–227 (2002)

[21] Ringsberg J W. Life prediction of rolling contact fatigue crack initiation. *Int J Fatigue* **23**(7): 575–586 (2001)

[22] Lemaitre J, Chaboche J L, Maji A K. Mechanics of solid materials. *J Eng Mech* **119**(3): 642–643 (1993)

[23] He H F, Liu H J, Zhu C C, Yuan L H. Shakedown analysis of a wind turbine gear considering strain-hardening and the initial residual stress. *J Mech Sci Technol* **32**(11): 5241–5250 (2018)

[24] He H F, Liu H J, Zhu C C, Wei P T, Tang J Y. Analysis of the fatigue crack initiation of a wind turbine gear considering load sequence effect. *Intl J Damage Mech* **29**(2): 207–225 (2020)

[25] He H F, Liu H J, Zhu C C, Wei P T, Sun Z D. Study of rolling contact fatigue behavior of a wind turbine gear based on damage-coupled elastic-plastic model. *Int J Mech Sci* **141**: 512–519 (2018)

[26] Hannes D, Alfredsson B. Surface initiated rolling contact fatigue based on the asperity point load mechanism–A parameter study. *Wear* **294–295**: 457–468 (2012)

[27] Suraratchai M, Limido J, Mabru C, Chieragatti R. Modelling the influence of machined surface roughness on the fatigue life of aluminium alloy. *Int J Fatigue* **30**(12): 2119–2126 (2008)

[28] Zhang J, Shaw B A. The effect of superfinishing on the contact fatigue of case carburised gears. *Appl Mech Mater* **86**: 348–351 (2011)

[29] Grzesik W, Żak K. Modification of surface finish produced by hard turning using superfinishing and burnishing operations. *J Mater Process Technol* **212**(1): 315–322 (2012)

[30] Liu C R, Mittal S. Single-step superfinishing using hard machining resulting in superior surface integrity. *J Manuf Syst* **14**(2): 129–133 (1995)

[31] Flodin A, Andersson S. Simulation of mild wear in spur gears. *Wear* **207**(1-2): 16–23 (1997)

[32] Leonard B D, Sadeghi F, Shinde S, Mittelbach M. A numerical and experimental investigation of fretting wear and a new procedure for fretting wear maps. *Tribol Trans* **55**(3): 313–324 (2012)

[33] El-Thalji I, Jantunen E. Dynamic modelling of wear evolution in rolling bearings. *Tribol Int* **84**: 90–99 (2015)

[34] Yuan Z, Wu Y H, Zhang K, Dragoi M V, Liu M H. Wear reliability of spur gear based on the cross-analysis method of a nonstationary random process. *Adv Mech Eng* **10**(12): 1–9 (2018)

[35] Garcin S, Fouvry S, Heredia S. A FEM fretting map modeling: Effect of surface wear on crack nucleation. *Wear* **330–331**: 145–159 (2015)

[36] Llavori I, Urchegui M A, Tato W, Gomez X. An all-in-one numerical methodology for fretting wear and fatigue life assessment. *Frattura Integrità Strutturale* **37**(10): 87–93 (2016)

[37] Leonard B D, Sadeghi F, Shinde S, Mittelbach M. Rough

surface and damage mechanics wear modeling using the combined finite-discrete element method. *Wear* **305**(1–2): 312–321 (2013)

[38] Ghosh A, Leonard B, Sadeghi F. A stress based damage mechanics model to simulate fretting wear of Hertzian line contact in partial slip. *Wear* **307**(1–2): 87–89 (2013)

[39] Shen F, Hu W P, Meng Q C. A damage mechanics approach to fretting fatigue life prediction with consideration of elastic–plastic damage model and wear. *Tribol Int* **82**: 176–190 (2015)

[40] Fletcher D I, Franklin F J, Kapoor A. Image analysis to reveal crack development using a computer simulation of wear and rolling contact fatigue. *Fatigue Fract Eng Mater Struct* **26**(10): 957–967 (2003)

[41] Mazzù A, Petrogalli C, Lancini M, Ghidini A, Faccoli M. Effect of wear on surface crack propagation in rail-wheel wet contact. *J Materials Eng Perform* **27**(2): 630–639 (2018)

[42] Prager W. The theory of plasticity: A survey of recent achievements. *Proc Inst Mech Eng* **169**(1): 41–57 (1955)

[43] Wang C H, Brown M W. A path-independent parameter for fatigue under proportional and non-proportional loading. *Fatigue Fract Eng Mater Struct* **16**(12): 1285–1297 (1993)

[44] Morrow J. Cyclic plastic strain energy and fatigue of metals. In *Internal Friction, Damping, and Cyclic Plasticity*. Lazan B J, Ed. West Conshohocken: American Society for Testing & Materials, 1965: 45–86.

[45] Timoshenko S P, Goodier J N. *Theory of Elasticity*. New York (USA): McGraw-Hill Book Co., 1970.

[46] Wilkins E W C. Cumulative damage in fatigue. In *Colloquium on Fatigue/Colloque de Fatigue/Kolloquium über Ermüdungsfestigkeit*. Weibull W, Odqvist F K G, Eds. Berlin: Springer, 1956: 321–332.

[47] Zhan Z X, Hu W P, Li B K, Zhang Y J, Meng Q C, Guan Z D. Continuum damage mechanics combined with the extended finite element method for the total life prediction of a metallic component. *Int J Mech Sci* **124–125**: 48–58 (2017)

[48] Zhou Y, Zhu C C, Gould B, Demas N G, Liu H J, Greco A C. The effect of contact severity on micropitting: Simulation and experiments. *Tribol Int* **138**: 463–472 (2019)

[49] Archard J F. Contact and rubbing of flat surfaces. *J Appl Phys* **24**(8): 981–988 (1953)

[50] Baümel Jr A, Seeger T, *Materials Data for Cyclic Loading. Supplement 1*. New York (USA): Elsevier, 1990.

[51] Hartley N E W, Hirvonen J K. Wear testing under high load conditions: The effect of "anti-scuff" additions to AISI 3135, 52100 and 9310 steels introduced by ion implantation and ion beam mixing. *Nucl Instrum Methods Phys Res* **209–210**: 933–940 (1983)

[52] Manigandan K, Srivatsan T S, Quick T, Freborg A M. The high cycle fatigue and final fracture behavior of alloy steel 9310 for use in performance-sensitive applications. In *Fatigue of Materials II: Advances and Emergences in Understanding*. Srivatsan T S, Imam M A, Srinivasan R, Eds. Cham: Springer, 2013: 211–232.

[53] Bajpai P, Kahraman A, Anderson N E. A surface wear prediction methodology for parallel-axis gear pairs. *J Tribol* **126**(3): 597–605 (2004)

[54] Zhang B Y, Liu H J, Zhu C C, Li Z M Q. Numerical simulation of competing mechanism between pitting and micro-pitting of a wind turbine gear considering surface roughness. *Eng Fail Anal* **104**: 1–12 (2019)

[55] Zhou Y, Zhu C C, Liu H J. A micropitting study considering rough sliding and mild wear. *Coatings* **9**(10): 639 (2019)

[56] Liu H L, Liu H J, Zhu C C, Tang J Y. Study on gear contact fatigue failure competition mechanism considering tooth wear evolution. *Tribol Int* **147**: 106277 (2020)

[57] Zhang B Y, Liu H J, Bai H Y, Zhu C C, Wu W. Ratchetting–multiaxial fatigue damage analysis in gear rolling contact considering tooth surface roughness. *Wear* **428–429**: 137–146 (2019)

[58] Yuan R, Li H Q, Huang H Z, Zhu S P, Li Y F. A new non-linear continuum damage mechanics model for the fatigue life prediction under variable loading. *Mechanics* **19**(5): 506–511 (2013)

[59] Gautam A, Ajit K P, Sarkar P K. Fatigue damage estimation through continuum damage mechanics. *Procedia Eng* **173**: 1567–1574 (2017)

[60] Shen F, Zhao B, Li L, Chua C K, Zhou K. Fatigue damage evolution and lifetime prediction of welded joints with the consideration of residual stresses and porosity. *Int J Fatigue* **103**: 272–279 (2017)

[61] Townsend D P, Bamberger E N, Zaretsky E V. Comparison of pitting fatigue life of ausforged and standard forged AISI M-50 and AISI 9310 spur gears. Washington: NASA Lewis Research Center, United States NASA-TN-D-8030, E-8258, 1975.

[62] Townsend D P, Patel P R. Surface fatigue life of CBN and vitreous ground carburized and hardened AISI 9310 spur gears. *Int J Fatigue* **11**(3): 210 (1989)

[63] Liu H J, Liu H L, Zhu C C, Zhou Y. A review on micropitting studies of steel gears. *Coatings* **9**(1): 42 (2019)

Boyu ZHANG. She has been studying as a doctoral student in the State Key Laboratory Mechanical Transmissions (SKLMT), Chongqing University, China since 2020. Her research interest includes gear contact fatigue and peening enhancement.

Huaiju LIU. He is currently working as an associate professor in the State Key Laboratory of Mechanical Transmissions (SKLMT), Chongqing University, China. He received the Ph.D. degree from the University of Warwick, UK, in 2013. His research fields include tribology and fatigue behaviors of mechanical elements.

Caichao ZHU. He is a professor in the State Key Laboratory of Mechanical Transmissions (SKLMT), Chongqing University, China. He received the Ph.D. degree from Chongqing University, China in 1998. His research mainly relates to the intelligent design and dynamic analysis of transmission systems.

Yibo GE. He is the founder of Shanghai Peentech Equipment Tech. Co., Ltd. He graduated from Shanghai University of Engineering Sciences. He is one of official trainers of MFN.